

1 © IWA Publishing [2018]. The definitive peer-reviewed and edited version of this article is
2 published in *Water Science Technology*, 26 April 2018; 2017 (1): 87–98,
3 <https://doi.org/10.2166/wst.2018.089> and is available at www.iwapublishing.com

4 **A comparative study of manhole hydraulics using** 5 **stereoscopic PIV and different RANS models**

6 Md Nazmul Azim Beg^{1*}, Rita F. Carvalho¹, Simon Tait², Wernher Brevis^{2,4}, Matteo Rubinato², Alma
7 Schellart², Jorge Leandro³

8 ¹ Department of Civil Engineering, University of Coimbra, Coimbra, Portugal

9 ² Department of Civil and Structural Engineering, University of Sheffield, Sheffield, UK

10 ³ Hydrology and River Basin Management, Technical University of Munich, Munich, Germany

11 ⁴ Department of Hydraulics and Environmental Engineering, Pontifical Catholic University of Chile, Santiago, Chile

12 * Corresponding author's e-mail: mnabeg@uc.pt

13 **Abstract**

14 Flows in manholes are complex and may include swirling and recirculation flow with significant
15 turbulence and vorticity. However, how these complex 3D flow patterns could generate different
16 energy losses and so affect flow quantity in the wider sewer network is unknown. In this work,
17 2D3C stereo Particle Image Velocimetry (PIV) measurements are made in a surcharged scaled
18 circular manhole. A CFD model in OpenFOAM[®] with four different Reynolds Averaged Navier
19 Stokes (RANS) turbulence model is constructed using a VOF model, to represent flows in this
20 manhole. Velocity profiles and pressure distributions from the models are compared with the
21 experimental data in view of finding the best modelling approach. It was found among four
22 different RANS models that the RNG k- ϵ and k- ω SST gave a better approximation for velocity and
23 pressure.

24 **Keywords**

25 Manhole, OpenFOAM[®], RANS model, Stereoscopic PIV, VOF

26 **Introduction**

27 Manholes are one of the most common features in urban drainage networks. They are located at
28 changes in slope and orientation of the sewer pipes, as well as at regular intervals along the pipes
29 to enable maintenance. The flow pattern in a manhole is complex, especially during high flows,
30 and involves several hydraulic phenomena such as local flow contraction, expansion, rotation,
31 recirculation as well as possible air entrainment and sediment mixing. These flow phenomena can
32 control the overall energy loss, transport and dispersion of solute and particulate materials in the
33 manhole structure. PIV measurement can provide a good representation of the complex velocity
34 field of a manhole. Previously Lau (2008) studied two-dimensional PIV in a surcharged scaled
35 manhole. Attempts to measure stereo PIV data in a scaled manhole are however new and to the
36 authors' knowledge, has not been done before. Several researchers studied flow patterns in
37 surcharged manholes using CFD models. Use of different RANS modelling approach like RNG k- ϵ

38 model (Lau, Stovin, et al., 2007), Realizable k- ϵ (Stovin, Bennett, et al., 2013), k- ω model
39 (Djordjević, Saul, et al., 2013) have been reported. A little research study has been conducted on
40 how these flow patterns could affect flow movement and flow quality in the wider piped network.
41 In the current work, the flow phenomena of a scaled manhole are measured by stereo Particle
42 Image Velocimetry (PIV) and modelled numerically using OpenFOAM® CFD tools. Four different
43 RANS models, i.e. RNG k- ϵ , Realizable k- ϵ , k- ω SST and Launder-Reece-Rodi (LRR) were used, and
44 the differences in flow structures among them were compared and discussed.

45 **Methods and Materials**

46 **Experimental model**

47 The experimental facility was installed in the Hydraulic Laboratory of the University of Sheffield. It
48 consists of a transparent acrylic circular scaled manhole, linked to a model catchment surface
49 (Rubinato, Martins, et al., 2017). The manhole has an inner diameter (Φ_m) of 240 mm and
50 connected with a 75 mm diameter (Φ_p) inlet-outlet pipes. Both pipes are co-axial, and the pipe
51 axis passes through the centre of the manhole vertical axis (Fig. 1). Two butterfly valves (one at
52 $>48\Phi_p$ upstream the manhole, the other one at $>87\Phi_p$ downstream the manhole) are used to
53 control the inflow and the water depth of the manhole respectively. The inflow was monitored
54 using an electromagnetic MAG flow meter fitted within the inlet sewer pipe ($10\Phi_p$ from the
55 butterfly inlet valve). The ratio of the manhole diameters to inlet pipe diameters (Φ_m/Φ_p) is 3.20.
56 Two Gems series pressure sensors (Product code 5000BGM7000G3000A, serial number 551362,
57 range 0-70 mb) were installed vertically at the inlet and outlet pipes, the first one at 350 mm
58 upstream from the centreline of the manhole, the second one, 520 mm downstream from the
59 centreline of the manhole by making a hole in the pipe of $\Phi = 5$ mm. They can measure
60 piezometric pressures for both free surface and pressure flow conditions within the inlet-outlet
61 pipes. These transducers were calibrated such that transducer output signal (4-20 mA) can be
62 directly related to gauge pressure. For the calibration of the pressure transmitter 10 different
63 water levels were measured (range 50 to 500 mm, no discharge) and checked with a point gauge.
64 Rubinato (2015) found an overall accuracy can be defined as ± 0.72 mm. A transparent measuring
65 tape was attached vertically to the manhole side in order to check the manhole water levels
66 during the experiments. The tape position was at the other side of the camera, keeping an equal
67 distance from both inlet and outlet.

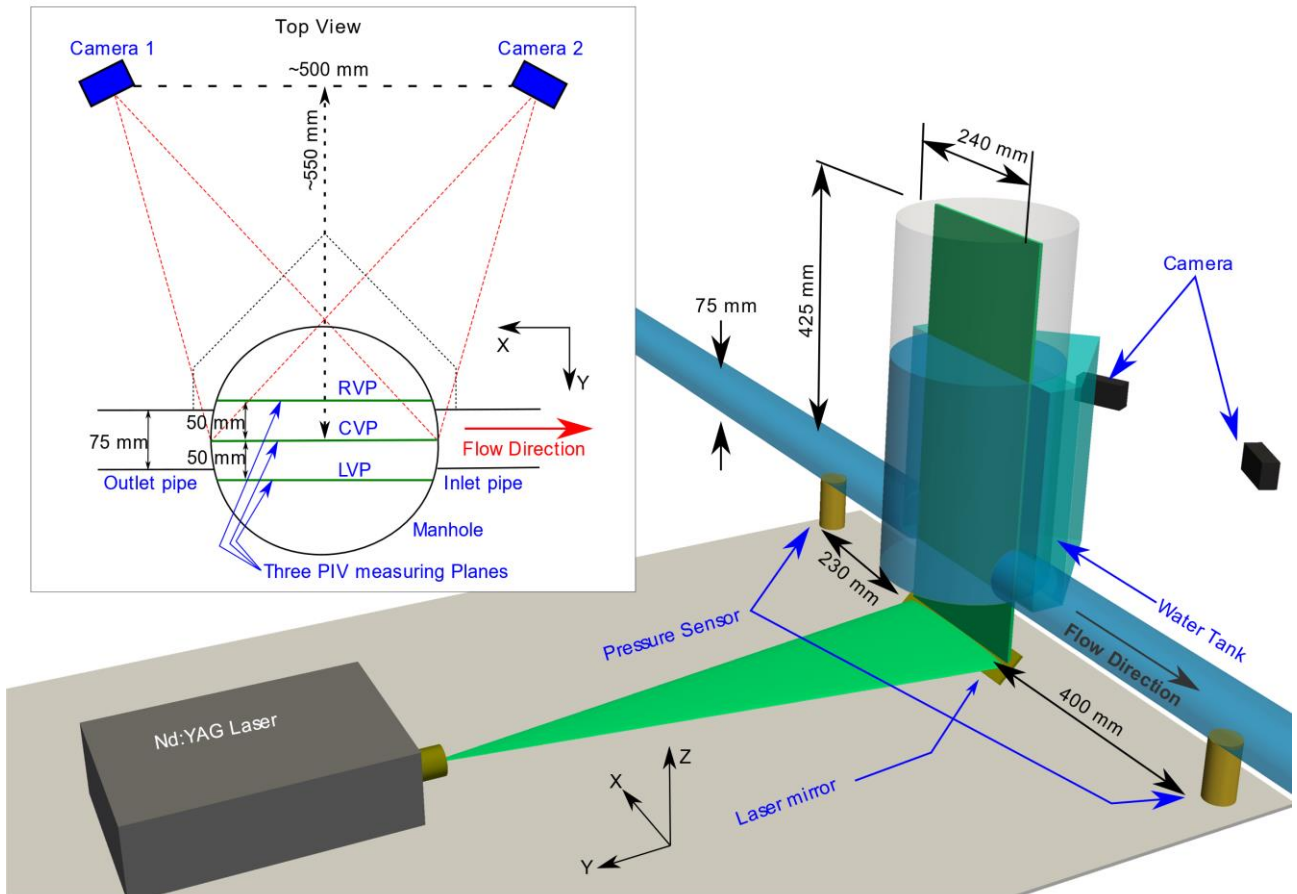


Fig. 1. Experimental setup for 2D3C stereo PIV measurement at the manhole

PIV measurement

A stereo PIV measurement setup was installed. Two Dantec FlowSense EO 2M cameras and an Nd:YAG pulsed laser was placed at opposite sides of the scaled manhole. Each camera resolution was 1600x1200 pixels (Fig. 1) and was set at the same distance from the manhole making more than 45° angle at the vertical centre of the measuring plane. To reduce error due to refraction through the curved manhole wall, a transparent acrylic tank was constructed around it and filled with water, keeping flat surfaces parallel to both camera lens axes. The laser was directed from the bottom of the acrylic manhole as a laser sheet with the help of a flat mirror set at 45° to the horizontal direction. The laser sheet thickness was around 4mm.

Conventional 2D PIV can give the velocity vectors perpendicular to the camera direction only, which is typically parallel to the laser sheet (known as the in-plane velocity (Leandro, Bung, et al., 2014)). However, the use of two cameras can give the reading of the third component of the velocity vector (referred as out of plane velocity) with proper regeneration of the 2D velocities from each camera images; provided that appropriate calibration is done beforehand. As both of the cameras see the same stationary image from two different angles, the calculated velocity vectors from the two successive snapshots of a moving particle will also orient differently on both cameras. This change in orientation is the result of the different camera position and out of the plane velocity vectors. If the camera position is known and distortion of a still image at each camera is known, the out of the plane velocity component can be calculated. Standard calibration plates were used in this study to calibrate the cameras.

90 When the manhole surcharge level is below a certain limit (typically around $0.2\Phi_m$), then the
91 manhole inlet flow reacts vigorously with the surface, creating irregular flow pattern and a very
92 high head loss. This surcharge limit is known as threshold surcharge (Stovin, Bennett, et al., 2013).
93 At higher surcharge, the flow pattern inside the manhole is regular. This work focuses to analyse
94 above threshold surcharge flow. The PIV measurements condition was chosen as $4 \text{ dm}^3/\text{s}$ of inflow
95 through the inlet pipe and a water level of 310 mm which resulted in a surcharge level of 235 mm
96 (s) at the manhole centre; making surcharge to manhole diameter ratio (s/Φ_m) 0.98. This was well
97 over the estimated threshold surcharge level. Initial inspection showed that the measurement
98 zone has two different distinctive velocity characteristics. One part of the measuring plane is
99 approximately in line with the inlet-outlet pipes and is characterised by a fast, slowly expanding jet
100 flow. The second part is outside the jet flow zone and is characterised by a recirculation in which
101 the velocity magnitude is around 10% of the jet flow. For these two distinctive velocity zones, data
102 were taken at different image time separation intervals ranging from 250 ms to 4000 ms; so that
103 velocities of both zones can be estimated accurately using the PIV cross-correlation algorithm.

104 For seeding, $100 \mu\text{m}$ polyamide 12 particles were chosen (density = 1010 kg/m^3). The particles
105 were mixed with water and kept in a seeding tank with continuous circulation so that they remain
106 in suspension. The particles were pumped from the seeding tank at a constant rate into the inlet
107 pipe approximately $40\Phi_p$ upstream on the manhole so that they were well mixed before entering
108 the manhole.

109 The seeding rate was adjusted by checking the PIV images to facilitate at least five particles in any
110 selected interrogation area. Data were recorded at three vertical planes; one passing through the
111 central axis of the inlet-outlet pipes and the other two at 50 mm offset from it (see Fig. 1). Each
112 data set was measured for five minutes, at a rate of 8 image pairs per second, totalling 2400 pairs
113 of images.

114 The data was analysed using Dantec Dynamics' DynamicStudio v3.31 software. The collected data
115 was pre-processed after masking the area of interest. The fluid velocity was calculated using an
116 adaptive cross-correlation technique keeping an interrogation area of 128×128 pixels with
117 consideration of 50% overlap between two adjacent areas. Median correction post-processing was
118 applied to remove erroneous vectors and which removed approximately 2 to 8% vectors from
119 each measurement set.

120 Due to the resolution and positioning of the laboratory setup, neither of the cameras was able to
121 cover the whole manhole height. Emphasis was given to the incoming jet to see how velocity is
122 distributed over the length of the manhole. Hence the data was recorded covering the lower zone
123 of the manhole; from the manhole bottom until the height of 150 mm of the manhole; which is
124 two times of the inlet-outlet pipe diameter.

125 Numerical model

126 The open source CFD model tool OpenFOAM®v4.1 was used in this work. The solver *interFoam* is
127 selected as it can predict the velocity patterns and the free-surface for sharp interfaces. This solver
128 uses a single set of Navier-Stokes/Reynolds-Average equations where the velocity is shared by
129 both phases and a Volume of Fluid (VOF) method (Hirt and Nichols, 1981) captures the free-

130 surface position. The length of the inlet pipe was chosen as 1000 mm (more than $13\Phi_p$) based on
131 some other previous works (Lau, 2008; Stovin, Bennett, et al., 2013), and the outlet pipe was kept
132 as 400 mm, which is until the position of the pressure sensor at the downstream of the manhole
133 (Fig. 2a). The computational mesh for the simulation was prepared with hexahedral Cartesian
134 mesh using *cfMesh* (Juretić, 2015).

135 Some pre-analysis of CFD simulations were performed in order to test the mesh independence.
136 For this case, three computational meshes were constructed having $dx = 2$ mm (Mesh 1), 4 mm
137 (Mesh 2) and 6 mm (Mesh 3) respectively keeping the global refinement ratio as 3. Number of
138 cells at these meshes are: 2.4 million, 861,500 and 380,000 respectively. The inlet flow condition
139 was prescribed as constant discharge of $Q = 4$ dm³/s. The meshes were simulated using k- ϵ
140 turbulence model and the velocity profiles at the manhole centre and at the outlet pipe were
141 extracted from the results (Fig. 2c). The mesh analysis was performed applying Richardson
142 extrapolation (Celik, Ghia, et al., 2008). The meshes gave similar results at the manhole jet zone
143 and at the pipe. However, the velocity profiles showed different results closed to the manhole
144 water surface (at around $z = 0.29$ m to 0.31 m) and close to the bottom (around $z = 0$ m). Mesh 3
145 predicted slightly slower velocity at the near surface zone. The apparent order (p) and the Grid
146 Convergence Index (GCI) was calculated at each grid point of the meshes. The average value of p
147 at the manhole centre and pipe were found 2.76 and 2.32 respectively. The GCI values were found
148 higher close to the surface and the walls. Analysis showed that 50% cells in the manhole has GCI
149 value below 10% when comparing Mesh 2 and Mesh 3; while 65% cell showed below 10% GCI in
150 case of comparing Mesh 1 and Mesh 2. However, in case of results at the pipe, 70% and 76% cells
151 showed GCI value below 10% in case of comparing Mesh 3-Mesh 2 and Mesh 2-Mesh 1
152 respectively. It was apparent that the results go towards mesh independence and Mesh 1 and
153 Mesh 2 show almost similar results. Average approximate relative error between Mesh 2 and
154 Mesh 1 was found to be 2.7%, whereas the simulation time requirement for Mesh 1 was more
155 than three times to that of Mesh 2. Considering the accuracy level and computational time
156 required, Mesh 2 with $dx = 4$ mm was found best suited for this work (y^+ is around 5).

157 The model considers all the manhole borders as *noSlip* wall (i.e. zero velocity at the wall) and three
158 open boundaries: *inlet*, *outlet* and *atmosphere* (Fig. 2b). Wall roughness was not considered as the
159 aim was to characterize the flow velocity patterns in the manhole in which the wall energy losses
160 were considered small in comparison with the entry, exit and mixing losses. The inlet boundary
161 conditions were prescribed as fixed velocity approving for fully developed pipe flow profile using
162 inverse power law of pipe flow (Çengel and Cimbala, 2006, chap. 8):

$$v_r = v_{max} \left(1 - \frac{r}{R}\right)^{1/n} \quad (1)$$

163 where v_r is the longitudinal velocity at a radial distance of r from the pipe axis, R is the pipe
164 radius, v_{max} is the maximum longitudinal velocity at the developed profile section and n is a
165 constant which is dependent on the Reynold's number of the flow. To find the best combination of
166 v_{max} and n , pre-analysis was done considering a pipe flow CFD model. The pipe diameter was
167 made the same as the inlet pipe ($\Phi_p=0.075$ m) and pipe length was kept 3 m ($40 \Phi_p$). The model
168 was simulated using k- ϵ model applying the same inflow ($Q = 4$ dm³/s). It was found that the pipe
169 becomes fully turbulent at flow reach of $27\Phi_p$ (2 m length) and after 20 s of simulation time. It

170 produces $v_{max} = 1.128\text{ms}^{-1}$ at fully turbulent condition and $n = 6.5$ gives the best fit curve of the
 171 development profile. These values were chosen to calculate inlet boundary condition of the
 172 manhole model using Eqn. 1. The outlet boundary condition was prescribed as fixed pressure
 173 boundary corresponding to average water column pressure head, measured with the outlet pipe
 174 pressure sensor (shown in Fig. 1). The pressure at atmosphere boundary condition (at the
 175 manhole top, shown at Fig. 2b) was prescribed as equal to *atmospheric pressure* and *zeroGradient*
 176 for velocity to have free air flow, if necessary.

177 The mentioned condition was simulated with four different Reynolds Average Navier-Stokes
 178 (RANS) turbulence modelling approaches; namely: RNG k- ϵ model, Realizable k- ϵ model, k- ω SST
 179 model and Launder-Reece-Rodi (LRR) model to evaluate if they are able to characterize the flow
 180 properly. The first two models use a two-equation based approach calculating turbulent kinetic
 181 energy (k) and turbulent energy dissipation (ϵ). These two models are and formulated by Yakhot,
 182 Thangam, et al. (1992) and Shih, Liou, et al. (1995) and known to be better than the standard k- ϵ
 183 model to give better prediction at separating flow and spreading rate of round jets respectively.
 184 The k- ω SST model used in OpenFOAM is based on Menter and Esch (2001) with updated
 185 coefficients from Menter, Kuntz, et al. (2003) and addition of the optional F3 term for rough walls
 186 (Hellsten, 1998). This model uses rate of dissipation (ω) instead of ϵ at the near wall zone and
 187 standard k- ϵ model at the zones far from the wall influence and is supposed to give better
 188 prediction at the near wall and turbulence separating flow. Wall-functions are applied in this
 189 implementation by using Kolmogorov-Prandtl expression for eddy viscosity (Hellsten, 1998) to
 190 specify the near-wall omega as appropriate. The blending functions are not currently used in
 191 OpenFOAM version because of the uncertainty in their origin. The effect is considered negligible in
 192 case of small y^+ cell at the wall (Greenshields, 2017) and hence can be applied to models with low
 193 y^+ cells. The fourth model uses the seven equation based Reynolds Stress Model (RSM); using
 194 turbulent kinetic energy (k) and six component of stress tensor (R) directly and therefore may
 195 predict complex interactions in turbulent flow fields in a better way. The initial condition was
 196 prescribed as filling the manhole up to the expected level. Inlet pipe, outlet pipe and the manhole
 197 zone in line with the inlet-outlet pipe was initialized with a fully developed velocity profile which
 198 was same as the inlet boundary condition. The inlet turbulent boundary and initial conditions k , ϵ ,
 199 R and ν_t were calculated using standard equations as follows:

$$k = \frac{3}{2} (I |\mathbf{u}_{ref}|)^2 \quad (2)$$

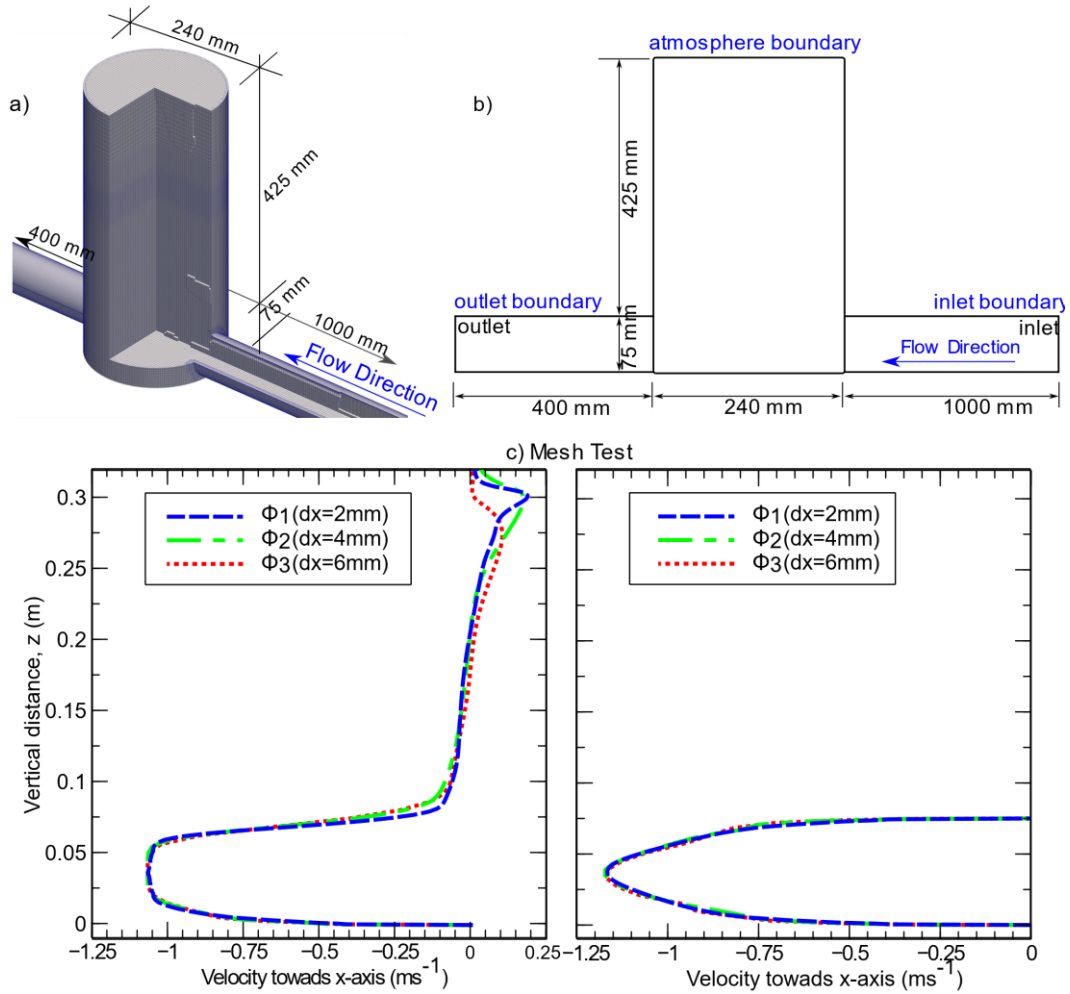
$$\epsilon = \frac{C_\mu^{0.75} k^{1.5}}{L} \quad (3)$$

$$\nu_t = C_\mu \frac{k^2}{\epsilon} \quad (4)$$

$$\omega = \frac{k^{0.5}}{C_\mu L} \quad (5)$$

200 where \mathbf{u}_{ref} is the velocity to be considered, I is the turbulent intensity (chosen as 0.05 at this
 201 case), C_μ is a constant (=0.09) and L is the characteristic length of the inlet pipe.

202 Standard wall function was considered in k- ω SST model only as according to the model
 203 description, it requires wall function for $y^+ > 1$. The rest of the models require wall function when
 204 $30 < y^+ < 300$.



205
206 *Fig. 2. a) Numerical model mesh (top left panel), b) Boundary locations (top right panel) and*
207 *c) Mesh convergence test (bottom panel)*

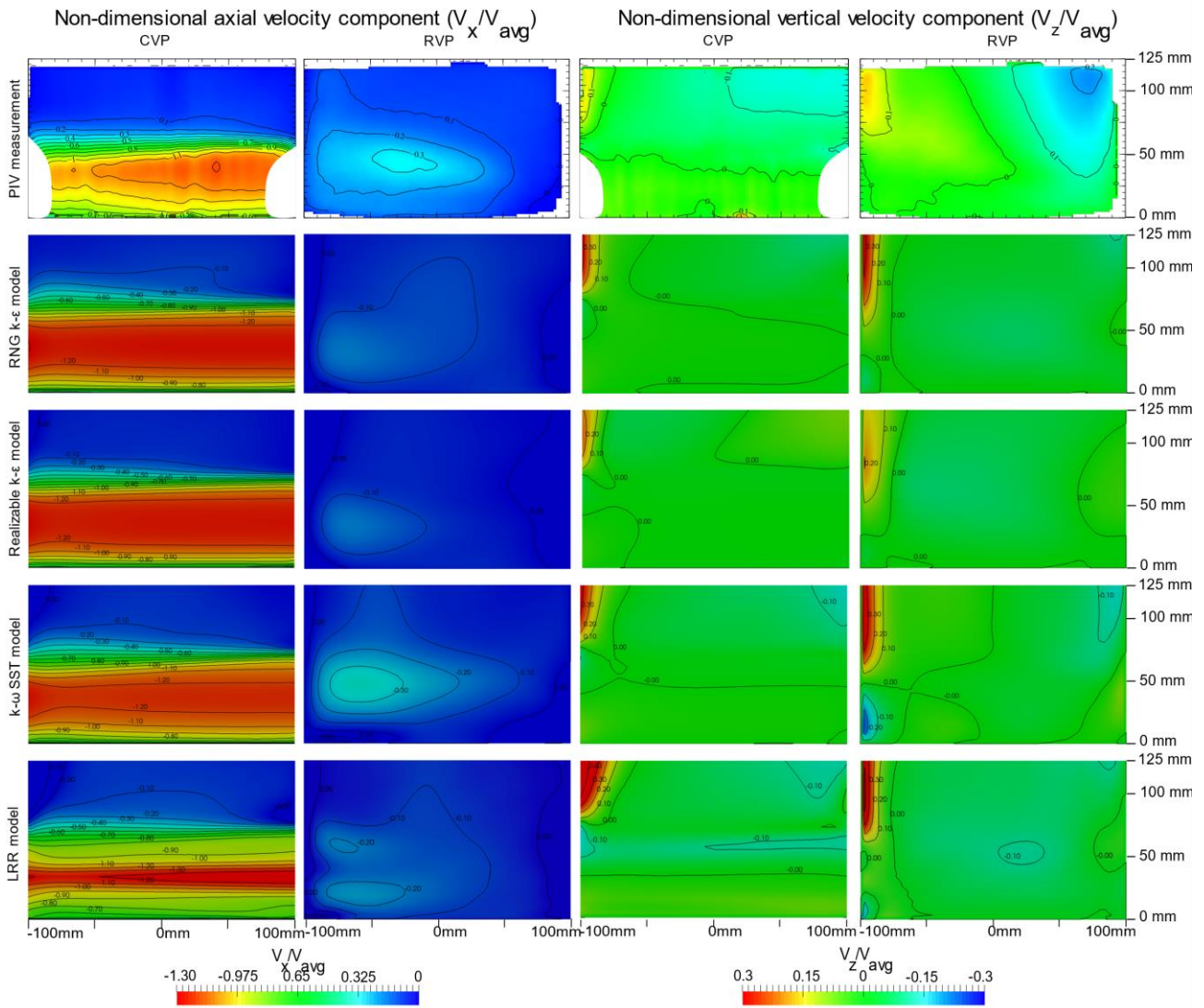
208 During the simulations, the *adjustableRunTime* code was used keeping maximum Courant–
209 Friedrichs–Lewy (CFL) number to 0.95. Cluster computing system at the University of Coimbra was
210 used to run the simulations using MPI mode. Each simulation was run for 65 seconds. The steady
211 condition was ensured by checking the residuals of p , α .water, k , ϵ and R_{xx} (where
212 applicable). The first 60 seconds were required to reach steady state condition and the results of
213 101 velocity profiles in the last 5 seconds were averaged and all the numerical analysis were made
214 using averaged data of these mentioned time step results.

215 Results and Discussion

216 The processed PIV velocity data were compared with velocity data of the manhole model. The PIV
217 measurement was taken at the central vertical plane (CVP) along with the left vertical plane (LVP)
218 and right vertical plane (RVP) (Fig. 1). However, the position of LVP was much further from the
219 camera, and light ray coming from the two edges of the LVP have to travel through the manhole
220 inlet-outlet pipe. Although the scaled manhole model is made of transparent acrylic, the joints
221 between the model components were semi-transparent to non-transparent. Due to this limitation,
222 the LVP image edges had bad data in some cases, as the camera could not see the seeding
223 particles due to the obstruction made by the model joints. So in this work, PIV data comparison is

224 only done to the CVP and RVP of the manhole. Fig. 3 shows the axial (V_x) and vertical (V_z) velocity
225 components comparison between the PIV data and numerical model results. All the comparison is
226 shown as dimensionless velocities as a ratio of the average inlet velocity (V_{avg}), where V_{avg} is the
227 ratio between inlet discharge (Q) and pipe cross section (A_p). Both PIV data and CFD data are
228 showing temporal mean velocities from the measurements and simulation results. PIV data at the
229 CVP near the manhole inlet and outlet pipe were not collected as it was not visible clearly by the
230 cameras due to the joints between pipe and manhole.

231 It can be seen from the velocity comparison at the CVP of PIV (1st and 3rd column of row 1 at Fig.
232 3), that the jet flow in the experimental results starts expanding slowly as it proceeds from the
233 inlet towards the outlet. The CVP axial velocity (V_x) (1st column of Fig. 3) reaches up to 110% of V_{avg}
234 at the experimental results. It dampens down at the manhole centre. The maximum velocity near
235 the outlet pipe is the same as V_{avg} . However, in the CFD data, this damping effect is not seen. The
236 high-velocity core stays as 110% of V_{avg} until it reaches the outlet. While the jet flow trying to
237 escape through the outlet pipe, it hits the manhole wall at the top of the outlet (near $x = -100$ mm
238 and $y = 75$ mm) and creates a vertically upward velocity component which is up to 20% of V_{avg} (3rd
239 column of Fig. 3). However, in all the CFD, the vertical velocity component at this zone reaches up
240 to 30% of V_{avg} . Comparing the velocity contours of V_x and V_z at the CVP, it can be seen that LRR
241 model could not predict the velocity profile properly. This model shows different axial velocity
242 contour at CVP which is dissimilar to PIV measurements.

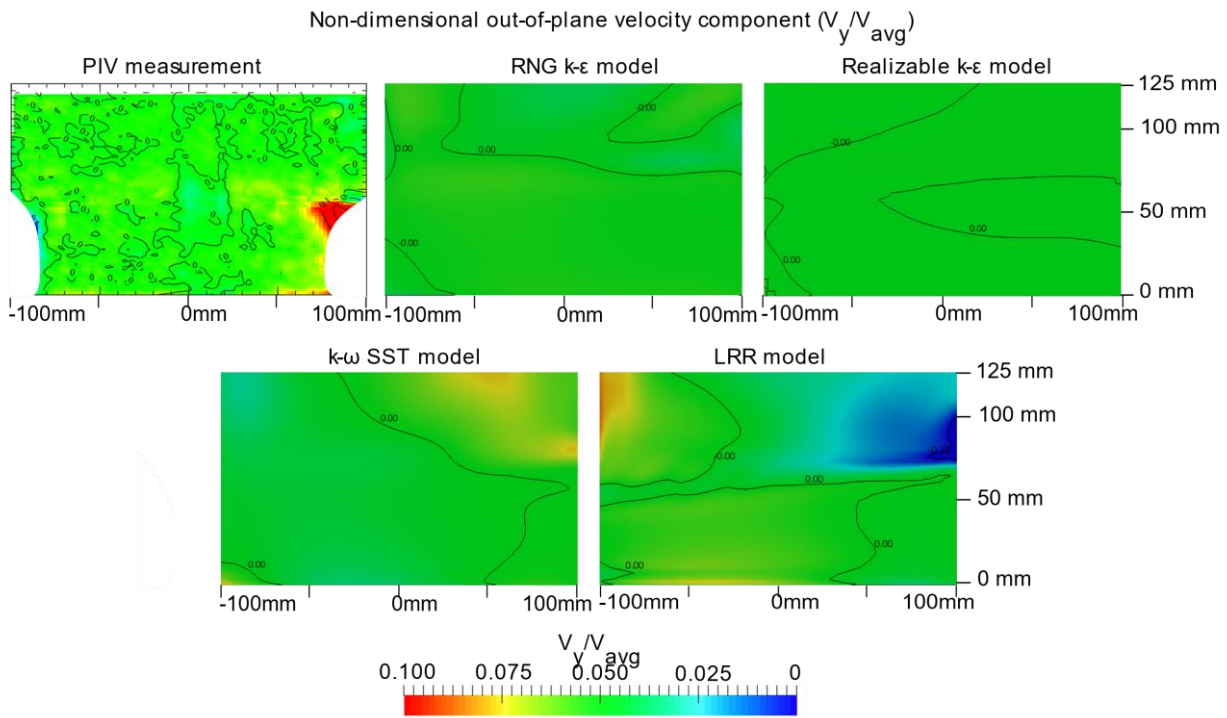


243

244 *Fig. 3. Comparison of non-dimensional velocity components from the numerical models and PIV*
 245 *measurement at both CVP and RVP of the manhole. The flow direction is from right to the left*

246 Comparing the velocity towards the pipe axis at the RVP (2nd column of Fig. 3), RNG k-ε and
 247 Realizable k-ε models slightly underestimate the axial velocity component in compared to the PIV
 248 experiment. The PIV data showed axial velocity up to $0.3V_{avg}$ whereas, in these two numerical
 249 models, the highest velocity is found $0.25V_{avg}$. The axial velocity at this plane is properly estimated
 250 by k-ω SST model. The shape of the velocity contour is almost similar to that of the PIV data. The
 251 vertical velocity component (V_z) (4th column of Fig. 3), at PIV is observed between $-0.2V_{avg}$ and
 252 $0.2V_{avg}$. The numerical models show similar results of V_z near the outlet of the manhole. However,
 253 at the upper part of the measuring plane near the inlet, the V_z was measured in PIV as around
 254 $-0.2V_{avg}$, which was not predicted by the numerical models. Only k-ω SST model in this plane shows
 255 a negative (downward) velocity near the inlet, however still underestimated than the PIV.

256 The velocity comparison was not done for out of the plane component (V_y) as at CVP, this
 257 component is very close to zero and considered not significant (Fig. 4).

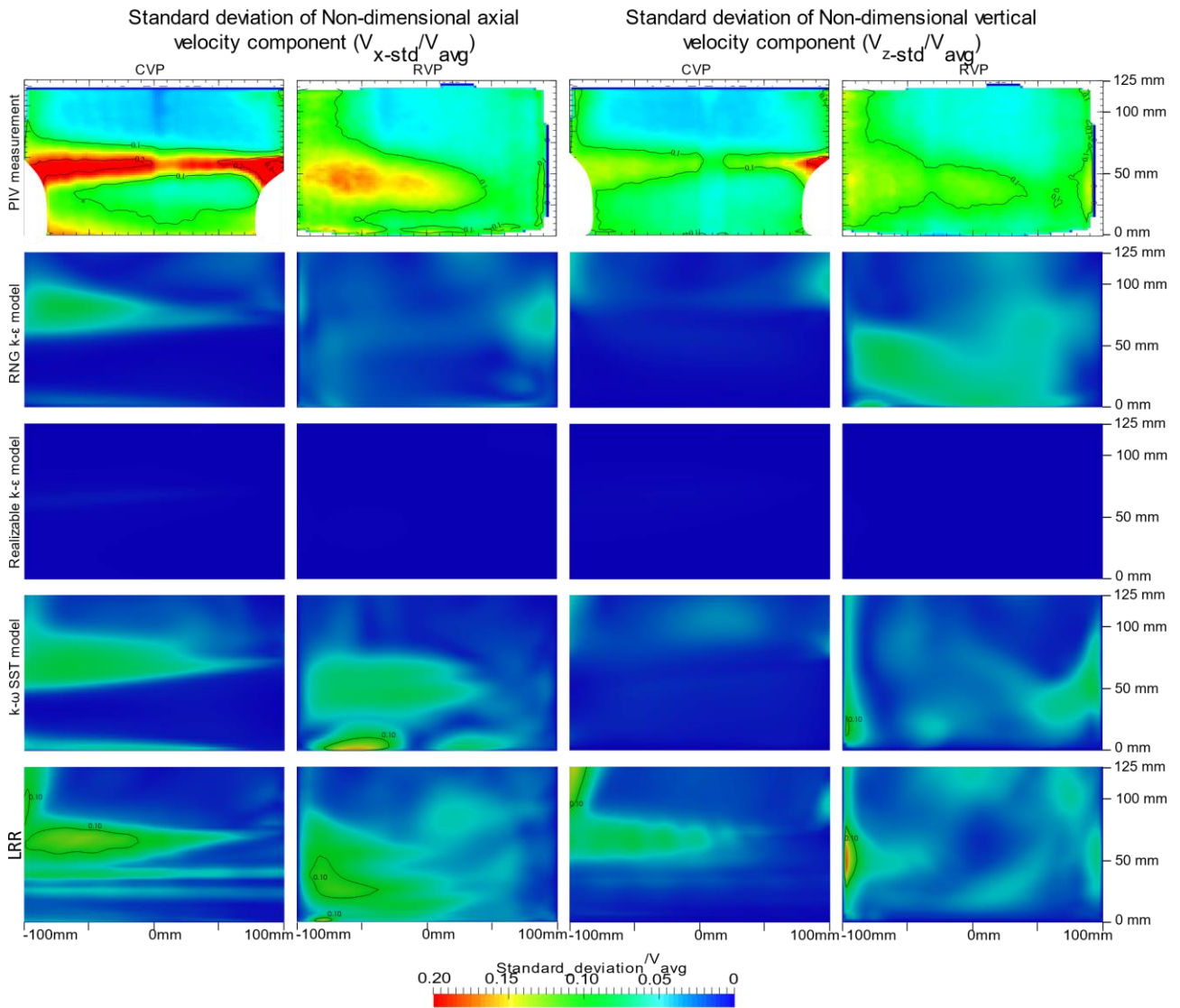


258
259 *Fig. 4. Out of the plane velocity component at the CVP from PIV and four RANS models*

260 The standard deviation of the data was also compared at both CVP and RVP for axial and vertical
261 velocity components (Fig. 5). The comparison was also made on dimensionless velocities as a ratio
262 of V_{avg} .

263 It can be seen that for axial velocity component (V_x) at CVP and RVP (1st and 2nd column at Fig. 5),
264 the PIV data shows high standard deviation near inlet, outlet and jet expansion zones. High
265 standard deviation can also be seen near the manhole floor of CVP. Vertical velocity component
266 (V_z) showed lower deviation compared to V_x . The standard deviation was found to be significantly
267 low at both planes in CFD results in compared to PIV data. All CFD results show marginally higher
268 standard deviation values close to the jet expansion zone. The Realizable k- ϵ model shows the
269 minimum fluctuation in the velocity fields, resulting almost zero standard deviation. The k- ω SST
270 model shows the highest standard deviation among all the four RANS models, still, the value is
271 lower than that of the PIV data. As these numerical models are formulated from Reynolds
272 Averaged Navier Stokes (RANS) equations, a big part of the turbulence variabilities is averaged out
273 from the results already. Perhaps Large Eddy Simulation (LES) model could show better standard
274 deviation match with the PIV data. Moreover, for this work, only 5 seconds of numerical
275 simulation data was considered. In case the longer period of data was taken into consideration,
276 probably the standard deviation in the CFD results would come higher. Turbulence coming from
277 pipe rather than the standard turbulence inlet conditions could also be a reason for the
278 differences in numeric.

279 Examining the velocity contours at Fig. 3 and Fig. 5, it can be stated that k- ω SST model creates the
280 closest approximation of the manhole velocity field followed by RNG k- ϵ model. The LRR model
281 overestimates the axial velocity component in this plane and the velocity contour is significantly
282 different than the PIV measurement.

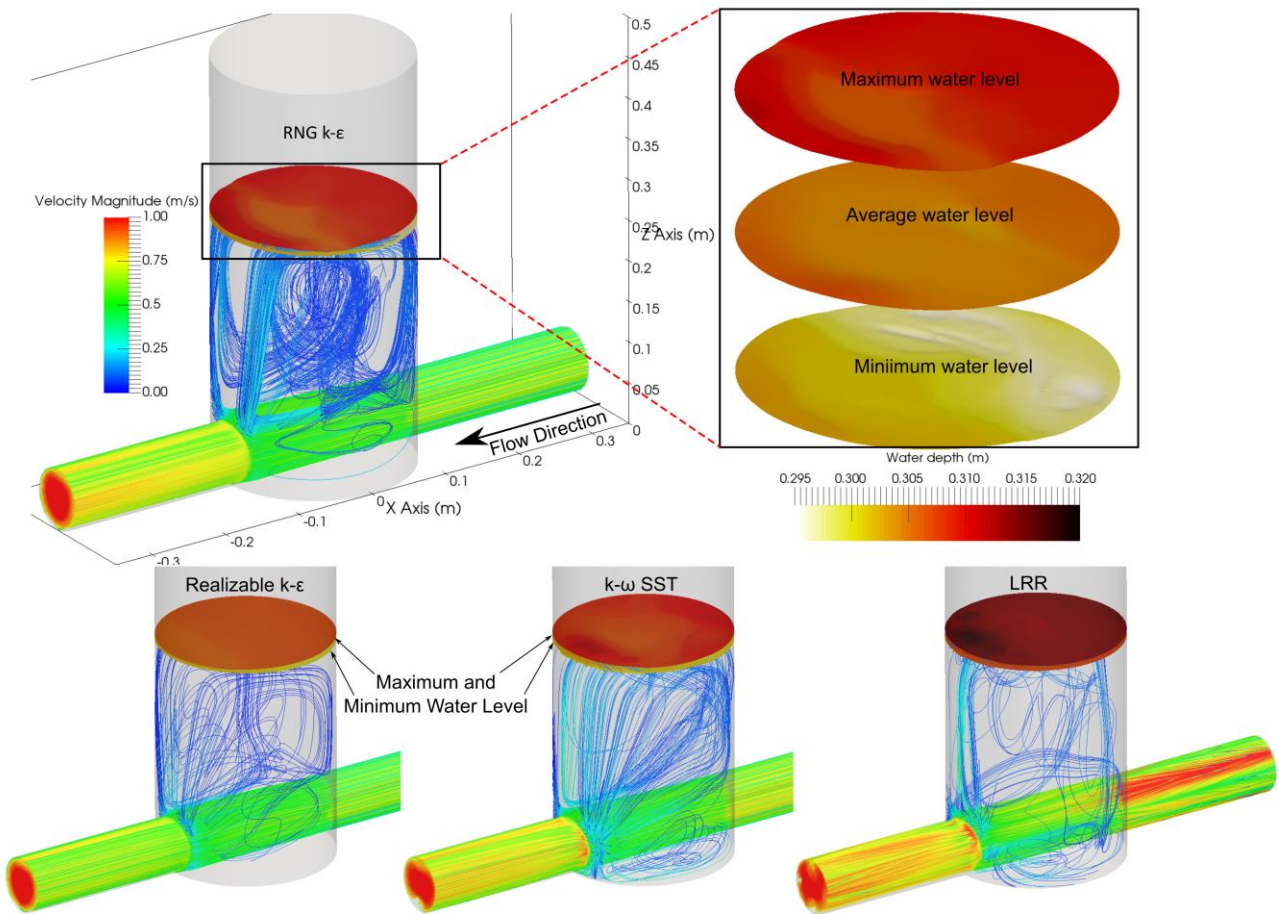


283

284 *Fig. 5. Temporal standard deviation of different velocity component at CVP and RVP, measured*
 285 *from PIV data and four RANS models*

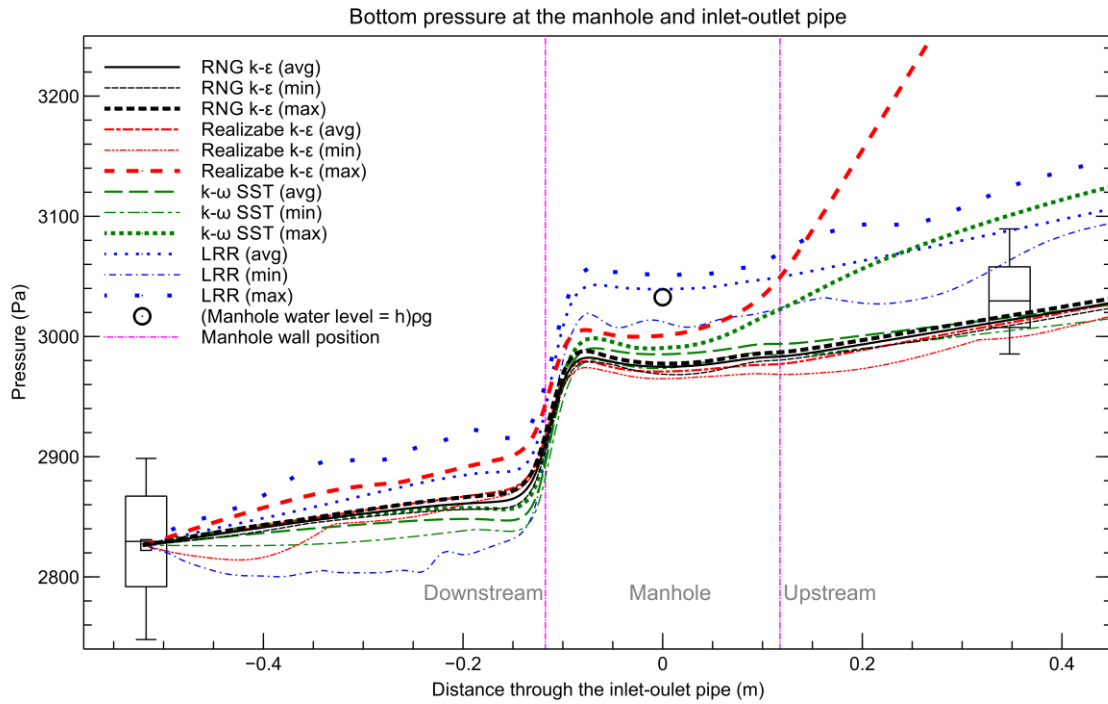
286 To understand the manhole flow more clearly, streamline and water level fluctuation was
 287 analysed from the numerical model results (Fig. 6). It can be seen that the inflow jet originating
 288 from the inlet, marginally spread in the manhole (termed as the diffusive region). When exiting
 289 the manhole through the outlet pipe, the diffusive region impinges the manhole wall and after
 290 that part of the jet flow moves vertically upward. This flow region reaches the manhole water
 291 surface, starts moving opposite to the core jet direction and makes a clockwise circulation. Due to
 292 this constant circulation, the free surface of the manhole fluctuates slightly. The fluctuation was
 293 found more towards the inlet of the manhole. In this case, the water level was observed varying
 294 between 0.295 m to 0.320 m. The fluctuation level was found different in the four numerical
 295 models. In RNG k-ε model, the water level varies from 0.300 m to 0.310 m. While the water level
 296 fluctuations in the other three manhole models were found as Realizable k-ε: varying between
 297 0.300 m and 0.305 m; k-ω SST: varying between 0.300 m and 0.310 m and LRR: varying between
 298 0.310 m and 0.320 m. In the experimental work the average water level at the manhole was
 299 observed as 0.310 m. The fluctuation of the manhole level was not possible to measure in the

300 experimental work as it would require installing a pressure sensor at the manhole bottom, which
 301 would create an obstacle in the laser ray path line and hence was not used.



302
 303 *Fig. 6. Flow streamline through the manhole and water level range from different models*

304 The pressure distributions in different CFD models were also compared with experimental data
 305 and can be seen in Fig. 7. All distances showed at the horizontal axis are measured from the
 306 manhole centre. The inlet and outlet pipes are connected at distance of 0.12 m and -0.12 m
 307 respectively. The bottom pressure in between these two distances also represents free surface
 308 water level inside the manhole. Two box plots represent pressure data recorded during the
 309 experimental measurement using pressure sensors. The left box plot shows the pressure at the
 310 outlet pipe, whose average value was used to generate boundary condition of the numerical
 311 models. As the downstream pressure is same for all the four models, all the model results pass
 312 through the average value of this box. Pressures at the upstream side were calculated from the
 313 models. All the line plots are showing maximum, minimum and average bottom pressure from
 314 each of the four CFD models. The circular marker at the manhole centre (at $x=0$ m) is showing the
 315 product of recorded average water height at the manhole during the experimental works ($h =$
 316 0.310 m), water density (ρ) and gravitational acceleration (g).



317

318 *Fig. 7. Bottom pressure comparison from different RANS models and the experimental pressure*
 319 *sensor data*

320 From Fig. 7, it can be seen that when the upstream flow through the inlet pipe enters the
 321 manhole, the flow experiences a pressure drop, which is due to the expansion of the flow. The
 322 second pressure drop can be observed when the flow exits the manhole and enters the outlet
 323 pipe. This drop is due to the flow contraction and much bigger in magnitude. The average pressure
 324 line of RNG k-ε, Realizable k-ε and k-ω SST models produce a similar pressure pattern throughout
 325 the computational domain. The LRR model overestimates the bottom pressure of the manhole,
 326 although the difference found is in the range of few millimetres of water column head. The
 327 maximum, minimum and the average bottom pressure from RNG k-ε model shows almost the
 328 same line which presents that the RNG k-ε model shows almost zero pressure fluctuation.
 329 Apparently, the LRR model overestimated the pipe loss in compared to the other three models.
 330 This results in an overestimation of upstream pressure at the inlet direction.

331 The coefficient of head loss (K) in the manhole is known as the ratio between head loss and the
 332 velocity head and is calculated using equation (6).

$$K = \Delta H / \left(\frac{v^2}{2g} \right) \quad (6)$$

333 where ΔH is the head loss, v is the average longitudinal velocity at the outlet pipe (= 0.89 m/s)
 334 and g is the acceleration due to gravity.

335 As the numerical model reached steady state before extracting any results, and as both inlet and
 336 outlet pipes were full, the temporal averaged velocity at each pipe can be considered equal. In this
 337 case, a difference in bottom pressure would give the same value as head loss. To compute the
 338 pressure drop at the manhole centre for a certain CFD result, each line showing the average
 339 bottom pressure (Fig. 7) was projected to the manhole centre from both inlet and outlet pipe. The

340 vertical difference of pressure value between these two lines at the manhole centre gives the
 341 value of pressure drop for the manhole, which is later divided by ρg and considered as ΔH .

342 The value of manhole head loss coefficient has been reported in different literature. This is directly
 343 related to the structural mould types of the manhole, manhole to pipe diameter ratios, as well as
 344 manhole surcharge ratio. A comparable analysis of the coefficients of head loss (K) with those of
 345 the values reported in different literature are shown in Tab. 1. It should be noted that only the
 346 research works reporting the same manhole mould type are considered here. In the work of both
 347 Arao and Kusuda (1999) and Lau, Stovin, et al. (2008), authors reported high head loss coefficient
 348 at below threshold surcharge conditions and comparably lower coefficient at above threshold
 349 surcharge condition. As in this research, the manhole surcharge condition is comparable to above
 350 threshold surcharge, only the coefficient range covering this condition are shown.

351 *Tab. 1. Different values of head loss coefficient (K) at different models*

Works done	Head loss coefficient	Experimental condition (Φ_m/Φ_p)	Surcharge ratio range	
			s/Φ_m	s/Φ_p
Marsalek (1981)	0.210	1.923		
Arao and Kusuda (1999)	0.18-0.58	3.60	0.55-1.67	2-6
Lau, Stovin, et al. (2008)	0.28-0.69	9.08	0.65-0.82	5.90-7.45
This work				
RNG k- ϵ	0.193			
Realizable k- ϵ	0.156			
k- ω SST	0.284	3.20	0.98	3.13
LRR	0.265			

352
 353 Tab. 1 shows that the four models calculate the manhole flow differently and hence give different
 354 values of manhole head loss coefficient. It is reported by different authors the head loss
 355 coefficient becomes higher when manhole to pipe diameter ratio (Φ_m/Φ_p) is high and vice versa
 356 (Stovin, Bennett, et al., 2013; Bo Pedersen and Mark, 1990). The manhole reported at Arao and
 357 Kusuda (1999) has a similar Φ_m/Φ_p . Comparing the findings from the literature, it is apparent the
 358 Realizable k- ϵ model gives rather low head loss coefficient for this case. From the rest three
 359 models, the coefficient given by k- ω SST model is almost 50% more than that of value given by
 360 RNG k- ϵ , however, both values lie within the range specified by other researchers.

361 **Conclusions**

362 In this work, two-dimensional three component (2D3C) stereo PIV measurement was done on a
 363 scaled inline manhole with manhole to pipe diameter ratio of 3.20, in order to evaluate CFD model
 364 constructed in OpenFOAM® and four different RANS models with VOF method. From the analysis,
 365 it can be apparent that each model calculates the velocity inside manhole differently. Comparison
 366 with PIV measurement at the central vertical plane showed similar velocity as compared to all the
 367 numerical models. However, comparison of the velocity at another vertical plane 50 mm offset to
 368 the centre, showed that all the CFD models slightly underpredicts the axial velocity. The velocity
 369 and locations of vortex structures centres were found marginally different among the models. The

370 k- ω SST model showed the closest approximation of velocity contour followed by the RNG k- ϵ
371 model. All the models showed very good approximations of the average water surface level at the
372 manhole. However, the LRR model could not quite capture the velocity profile in compared to PIV
373 data. This model predicts considerably higher axial velocities for central vertical plane as
374 compared to PIV. Nonetheless, the temporal standard deviations of the axial and vertical velocity
375 components were found significantly low when compared to those of experimental measurement
376 through PIV. As a RANS model is formulated based on time-averaged turbulence data, which could
377 be the reason of having a lower standard deviation in the CFD model.

378 Bottom pressure analysis through the computational domain shows that the average pressure line
379 is almost similar at RNG k- ϵ , Realizable k- ϵ and k- ω SST models. However, the comparison could be
380 made with data from only two pressure sensors installed at the inlet and outlet pipe respectively.
381 RNG k- ϵ model showed almost no pressure fluctuation while maximum pressure line predicted by
382 the Realizable k- ϵ model was found much higher than the measurement. The calculated head loss
383 coefficients were compared with the values reported in the literature. It was seen that the
384 Realizable k- ϵ model shows much lower value compared to the values reported.

385 Considering all the aspects of the four models analysed here, it can be said that both RNG k- ϵ
386 model and k- ω SST models give a very good approximation of manhole hydraulics. However, it
387 should be noted while using k- ω SST model, the wall boundary cell size must be made considerably
388 small for the proper formulation of the model.

389 **Acknowledgement**

390 The work presented is part of the QUICS (Quantifying Uncertainty in Integrated Catchment
391 Studies) project. This project has received funding from the European Union's Seventh Framework
392 Programme for research, technological development and demonstration under grant agreement
393 No. 607000. The laboratory facility was made possible through EPSRC, project EP/K040405/1. All
394 the numerical results here showed were performed on the Centaurus Cluster of the Laboratory for
395 Advanced Computing of University of Coimbra, Portugal.

396 **References**

- 397 Arao, S. & Kusuda, T. 1999 Effects of pipe bending angle on energy losses at two-way circular drop
398 manholes. In: *8th International Conference on Urban Storm Drainage. Sydney, Australia, 8th*
399 *International Conference on Urban Storm Drainage*, pp. 2163–2168.
- 400 Bo Pedersen, F. & Mark, O. 1990 Head losses in sewer manholes: submerged Jet Theory. *Journal of*
401 *Hydraulic Engineering* **116** (11), 1317–1328.
- 402 Celik, I. B., Ghia, U., Roache, P. J., Freitas, C. J., Coleman, H. & Raad, P. E. 2008 Procedure for
403 estimation and reporting of uncertainty due to discretization in CFD applications. *Journal of*
404 *Fluids Engineering* **130** (7), 78001.
- 405 Çengel, Y. A. & Cimbala, J. M. 2006 Flow in pipes. In: *Fluid Mechanics* (S. Jeans, ed.). McGraw-Hill,
406 New York, NY, USA.

- 407 Djordjevic', S., Saul, A. J., Tabor, G. R., Blanksby, J., Galambos, I., Sabtu, N. & Sailor, G. 2013
 408 Experimental and numerical investigation of interactions between above and below ground
 409 drainage systems. *Water Science and Technology* **67** (3), 535–542.
- 410 Greenshields, C. J. 2017 *OpenFOAM User Guide v5.0*.
- 411 Hellsten, A. 1998 Some Improvements in Menter's k-omega-SST turbulence model. In: *29th AIAA*
 412 *Fluid Dynamics Conference*, Albuquerque, New Mexico, U.S.A., pp. 1–11.
- 413 Hirt, C. W. & Nichols, B. D. 1981 Volume of fluid (VOF) method for the dynamics of free
 414 boundaries. *Journal of Computational Physics* **39** (1), 201–225.
- 415 Juretic', F. 2015 *cfMesh User Guide (v1.1)*. Zagreb, Croatia.
- 416 Lau, S. D. 2008 *Scaling Dispersion Processes in Surcharged Manholes*. PhD Thesis, Department of
 417 Civil and Structural Engineering, University of Sheffield, Sheffield, UK.
- 418 Lau, S. D., Stovin, V. R. & Guymer, I. 2007 The prediction of solute transport in surcharged
 419 manholes using CFD. *Water Science and Technology* **55** (4), 57–64.
- 420 Lau, S.-T. D., Stovin, V. R. & Guymer, I. 2008 Scaling the solute transport characteristics of a
 421 surcharged manhole. *Urban Water Journal* **5** (1), 33–42.
- 422 Leandro, J., Bung, D. B. & Carvalho, R. 2014 Measuring void fraction and velocity fields of a
 423 stepped spillway for skimming flow using non-intrusive methods. *Experiments in Fluids* **55**
 424 (5), 1–17.
- 425 Marsalek, J. 1981 *Energy Losses at Straight-Flow-Through Sewer Junctions*. Ministry of the
 426 Environment, Ottawa, ON, Canada.
- 427 Menter, F. & Esch, T. 2001 Elements of Industrial heat transfer. In: *16th Brazilian Congress of*
 428 *Mechanical Engineering (COBEM)*. Uberlândia, Brasil, COBEM, pp. 117–127.
- 429 Menter, F. R., Kuntz, M. & Langtry, R. 2003 Ten Years of Industrial Experience with the SST
 430 Turbulence Model. In: *Turbulence Heat and Mass Transfer 4* (K. Hanjalic, Y. Nagano & M.
 431 Tummers, eds). Begell House, Inc., Antalya, Turkey, pp. 625–632.
- 432 Rubinato, M. 2015 *Physical Scale Modelling of Urban Flood Systems*. PhD Thesis, Department of
 433 Civil and Structural Engineering, University of Sheffield, Sheffield, UK.
- 434 Rubinato, M., Martins, R., Kesserwani, G., Leandro, J., Djordjevic', S. & Shucksmith, J. 2017
 435 Experimental calibration and validation of sewer/surface flow exchange equations in steady
 436 and unsteady flow conditions. *Journal of Hydrology* **552**, 421–432.
- 437 Shih, T.-H., Liou, W. W., Shabbir, A., Yang, Z. & Zhu, J. 1995 A new k-e eddy viscosity model for high
 438 Reynolds number turbulent flows. *Computers Fluids* **24** (3), 227–238.
- 439 Stovin, V. R., Bennett, P. & Guymer, I. 2013 Absence of a hydraulic threshold in small-diameter
 440 surcharged manholes. *ASCE Journal of Hydraulic Engineering* **139** (September), 984–994.
- 441 Yakhot, V., Thangam, S., Gatski, T. B., Orszag, S. A. & Speziale, C. G. 1992 Development of
 442 turbulence models for shear flows by a double expansion technique. *Physics of Fluids* **4** (7),
 443 1510–1520

